Editors' Suggestion

All-Microwave Control and Dispersive Readout of Gate-Defined Quantum Dot Qubits in Circuit Quantum Electrodynamics

P. Scarlino, D. J. van Woerkom, A. Stockklauser, J. V. Koski, M. C. Collodo, S. Gasparinetti, C. Reichl, W. Wegscheider, T. Ihn, K. Ensslin, and A. Wallraff
Department of Physics, ETH Zurich, CH-8093 Zurich, Switzerland

(Received 14 November 2017; revised manuscript received 31 January 2019; published 22 May 2019)

Developing fast and accurate control and readout techniques is an important challenge in quantum information processing with semiconductor qubits. Here, we study the dynamics and the coherence properties of a GaAs/AlGaAs double quantum dot charge qubit strongly coupled to a frequency-tunable high-impedance resonator. We drive qubit transitions with synthesized microwave pulses and perform qubit readout through the state-dependent frequency shift imparted by the qubit on the dispersively coupled resonator. We perform Rabi oscillation, Ramsey fringe, energy relaxation, and Hahn-echo measurements and find significantly reduced decoherence rates down to $\gamma_2/2\pi \sim 3$ MHz corresponding to coherence times of up to $T_2 \sim 50$ ns for charge states in gate-defined quantum dot qubits. We realize Rabi π pulses of width down to $\sigma \sim 0.25$ ns.

DOI: 10.1103/PhysRevLett.122.206802

Fundamental and applied research on semiconductor quantum dots [1–3] attracts much attention largely due to the potential of using the electron charge [4,5] and spin [6,7] degrees of freedom as information carriers in solid state qubits. In practice, the coherence of both spin and charge qubits is limited by charge noise [4,8–12]. As a consequence, both improving coherence properties and reducing the timescale for the control and readout of qubits are important topics of current research, as they are crucial for realizing quantum information processing in such systems.

In this work, we address the control and readout challenges by making use of strong coherent coupling between charges in double quantum dots and photons stored in an on-chip resonator using the circuit QED architecture realized first with superconducting qubits [13] and more recently in silicon- [14], GaAs- [15], and carbon-based [16] quantum nanostructures. The techniques presented here apply also to electron-hole spin systems confined in quantum dots, for which the strong coupling regime has been recently achieved [17–19]. We use nonresonant (dispersive) interactions between a double quantum dot (DQD) charge qubit and a high impedance resonator for the time-resolved readout of the qubit coherently manipulated using microwave pulses.

In a more conventional approach, in which DQD charge qubits are manipulated using nonadiabatic pulses and read out by capacitively coupled charge detectors, T_2 coherence times of up to (7 ± 2.5) ns in GaAs [8] and (2.1 ± 0.4) ns in Si [20] have been observed. Spin-echo experiments performed with nonadiabatic pulses [21] found echo times of $T_{2,\mathrm{echo}} \sim (1.4 \pm 0.4)$ ns in GaAs [22] and Si [20]. Recently, first microwave-driven coherent operations showed improved qubit control and $T_{2,\mathrm{echo}} \sim (2.2 \pm 0.1)$ ns in three electron DQDs in SiGe [23], which is operated as a hybrid spin and charge qubit. In a more recent work, the free induction decay time of this system has been extended to $T_2 \sim 177$ ns through operation in the spinlike operating region [24].

Here, we perform experiments with a superconducting high-impedance resonator coupled to a DQD charge qubit [15]. The high-impedance resonator, which boosts the coupling strength and is frequency tunable, is composed of an array of 32 superconducting quantum interference devices (SQUIDs) [Fig. 1(a)] grounded at one end and terminated at the other end by a small island that is capacitively coupled to a coplanar waveguide used as a drive line. A gate line [red in Fig. 1(b)] extends from the island towards the DQD forming one of its plunger gates. The DQD is defined using voltage-biased aluminum (Al) depletion gates [3] connected to gold (Au) leads deposited on a small mesa etched into a GaAs/AlGaAs heterostructure forming a two-dimensional electron gas 90 nm below the surface [Figs. 1(a) and 1(b)]. We estimate an electron number of around 10 in each QD from the respective charging energies ($E_{c,1} \sim E_{c,2} \sim E_{c,m} \sim 100$ GHz) [3]. The device is operated in a dilution refrigerator at a temperature of ~30 mK.

We control the DQD qubit transition frequency $\nu_q = \sqrt{4t^2 + \delta^2}$ by tuning the interdot tunnel rate $2t$ to 3.71 GHz and by adjusting the detuning δ by applying bias voltages to the respective gates [25]. We tune the resonator frequency to $\nu_r(\Phi \approx 0.3\Phi_0) = 5.07$ GHz using externally applied magnetic flux Φ [15]. Sweeping the DQD detuning δ,

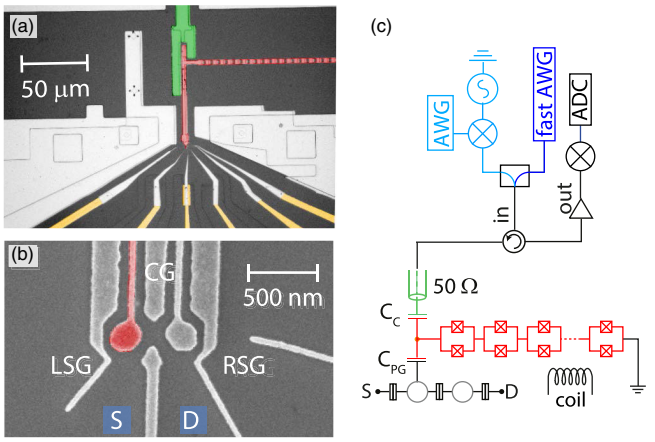

FIG. 1. Sample and simplified circuit diagram. (a) Optical micrograph of the device showing the substrate (dark gray), the Au gate leads (yellow), the superconducting structures including the Al fine gate structure forming the DQD (light gray), the SQUID array (red), and the microwave feed line (green). (b) SEM micrograph of the DQD showing its superconducting Al top gates (gray) and the plunger gate coupled to the resonator (red). (c) Circuit diagram schematically displaying the DQD source contact (S), drain contact (D), and coupling capacitance to the resonator (C_{PG}) and essential components in the microwave detection chain (circulator, amplifier, mixers, AWGs, microwave sources) used for performing reflectance measurements on the device. Boxes with crosses and rectangles indicate Josephson and normal tunnel junctions, respectively.

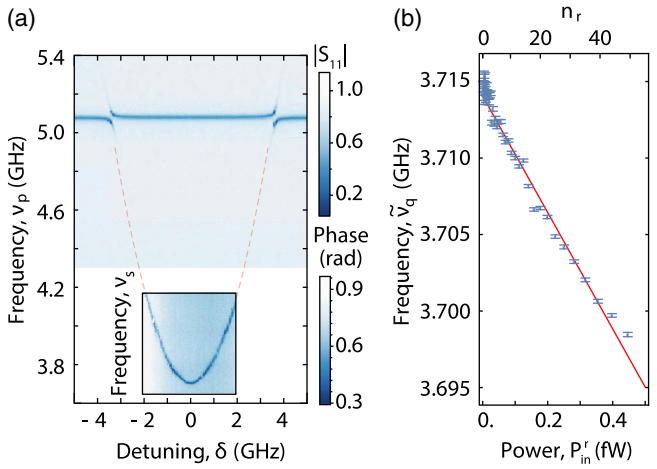

FIG. 2. Resonator and two-tone DQD charge qubit spectroscopy. (a) Resonator reflection response $|S_{11}|$ and qubit spectroscopy (inset: phase response of the microwave tone applied at the resonator frequency) versus DQD detuning δ, with $2t = 3.71$ GHz, $\nu_r(\Phi \approx 0.3\Phi_0) = 5.070$ GHz, and $2g/2\pi = 75$ MHz. (b) ac Stark shift of the DQD at $\delta = 0$ as a function of the power P^r_{in} at the resonator input, applied at the resonator frequency $\nu_p = \nu_r = 5.070$ GHz. Measured DQD qubit frequency $\tilde{\nu}_q = \nu_q(P_s \to 0) + 2n_r g^2/(2\pi\Delta_{r,q})$ and fit (solid line) versus P^r_{in}. The intraresonator photon number n_r extracted from the fit is indicated on the top axis.

the reflectance spectrum $|S_{11}(\nu_p)|$ [Fig. 2(a)] shows clear avoided crossings, which are the signature of strong coupling at resonance $\nu_q = \nu_r$ [14,15].

We measure a resonator linewidth of $\kappa_{\text{tot}}/2\pi = \kappa_{\text{ext}}/2\pi + \kappa_{\text{int}}/2\pi \sim (23 + 7)$ MHz $= 30$ MHz with external coupling κ_{ext} exceeding the internal losses κ_{int} realizing the overcoupled regime. From the vacuum Rabi splitting we extract a coherent coupling strength of $g/2\pi \sim 57$ MHz between the resonator and the DQD at resonance for $\nu_q(\delta = 0) = 2t \sim \nu_r = 5.695$ GHz [15].

When the DQD transition frequency ν_q is detuned by $\Delta_{r,q}/2\pi = \nu_q - \nu_r \gg g$, the resonator frequency $\tilde{\nu}_r = \nu_r \pm g^2/(2\pi\Delta_{r,q})$ is dispersively shifted conditioned on the qubit state [26]. We infer the qubit transition frequency from the detected phase shift of the resonator reflectance [14,15], as routinely used for superconducting qubits [27]. We perform continuous wave (cw) two-tone spectroscopy of the DQD charge qubit [13,27] by probing the amplitude and phase ($|\Delta\phi| = \tan^{-1}[2g^2/(\kappa_{\text{tot}}\Delta_{r,q})]$) of the resonator reflectance at fixed measurement frequency $\nu_p = \nu_r = 5.07$ GHz while applying an additional spectroscopy tone at frequency ν_s through the resonator to the DQD qubit [15]. The spectroscopically extracted transition frequency displayed in the lower part in Fig. 2(a) is in good agreement with the calculated qubit frequency $\nu_q = \sqrt{4t^2 + \delta^2}$ (red dashed line) for $2t = 3.71$ GHz.

The dispersive coupling leads to a qubit frequency shift $2n_r g^2/\Delta_{r,q}$, known as the ac Stark shift [26], dependent on the average resonator photon number n_r [27]. As expected, the qubit frequency $\tilde{\nu}_q = \nu_q + (1 + 2n_r)g^2/(2\pi\Delta_{r,q})$, measured in two-tone spectroscopy with low spectroscopy power ($P_s \to 0$), depends linearly on the resonator drive power P^r_{in} [Fig. 2(b)]. Using the independently determined coupling constant g and detuning $\Delta_{r,q}$ [Fig. 2(a)], we calibrate the average photon number n_r in the resonator versus input power P^r_{in} from the observed linear shift of the qubit frequency [Fig. 2(b)] [27].

From the dependence of the qubit linewidth $\delta\nu_q$ on the spectroscopy power (P_s) [15] at $2t \sim 3.3$ GHz and $\delta = 0$, we extract the qubit decoherence rate $\gamma_2(P_s \to 0)/2\pi = \gamma_1/4\pi + \gamma_\phi/2\pi = (3.3 \pm 0.2)$ MHz corresponding to $T_2 \sim (48 \pm 2)$ ns (see Fig. S2 in Ref. [28]). This rate is almost 10 times lower than previously reported values in similar GaAs-based devices [15] and is comparable to decoherence rates found for DQD charge qubits in undoped SiGe heterostructures [14].

We perform two-tone spectroscopy to study the dependence of the charge qubit linewidth on the DQD detuning δ. The qubit linewidth at $\delta = 0$ [red arrows in Fig. 3(a)] and around $+1$ and -2 GHz [blue and green arrows in Fig. 3(a), respectively] is observed to strongly increase with δ [Fig. 3(b)]. We extract the half width at half maximum (HWHM) $\delta\nu_q$ from fits to Lorentzians [solid line in Fig. 3(b)] and find that the qubit linewidth increases

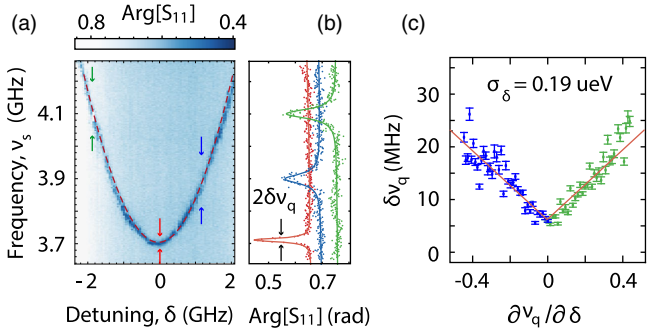

FIG. 3. Spectroscopy of the DQD charge qubit. Estimate of detuning noise. (a) Phase $\mathrm{Arg}[S_{11}]$ of a fixed frequency measurement tone $\nu_p = 5.070$ GHz reflected off the resonator versus qubit spectroscopy frequency ν_s and qubit detuning δ. Probe power $P_p = -35$ dBm at the generator ($n_r \sim 1$). The red dashed line is a fit to the qubit transition frequency with $2t = 3.71$ GHz. (b) Measurement of the DQD qubit linewidth at detunings indicated by the arrows in (a). The solid lines are fits to Lorentzians with HWHM $\delta\nu_q$. (c) $\delta\nu_q$ as a function of $\partial\nu_q/\partial\delta$ extracted from (a). The red lines are linear fits to Eq. (1) for positive and negative detuning.

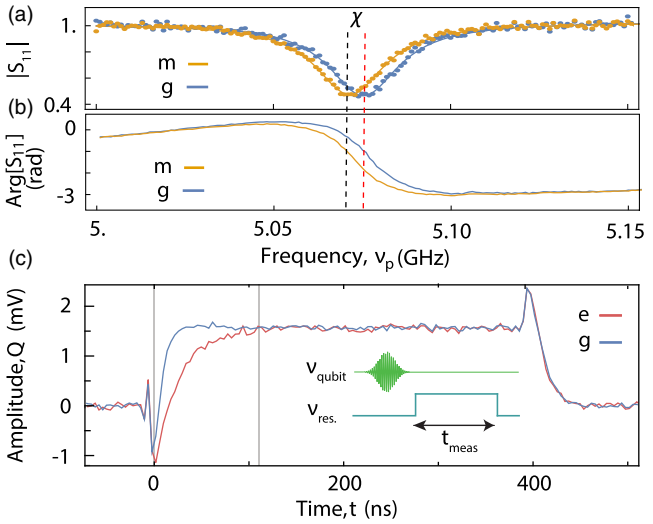

FIG. 4. Resonator response versus measurement frequency ν_p and time. (a) Amplitude $\mathrm{Abs}[S_{11}]$ and (b) phase $\mathrm{Arg}[S_{11}]$ of the resonator reflectance with no qubit drive tone applied (blue) (g) and with a continues tone (orange) at ν_q resulting in a mixed state (m) with parameters $\nu_q = 5.68$ GHz, $g/2\pi \sim 55$ MHz, and $\chi/2\pi \sim 5$ MHz. The vertical dashed red line indicates the resonator readout frequency selected for the time-resolved measurements in (c). (c) Time-domain response of the Q quadrature of the resonator reflectance with no pulse ($|g\rangle$, blue curve) and a π pulse ($|e\rangle$, red curve) applied at ν_q, respectively, before the readout. The integration window is indicated by vertical gray lines [33,34]. The inset shows the pulse sequence. The typical resonator readout pulse length is $t_{\mathrm{meas}} = 400$ ns.

linearly in $\partial\nu_q/\partial\delta$, broadening already by more than a factor of 5 at $|\delta| \sim 2$ GHz.

For Gaussian fluctuations of the detuning parameter with a standard deviation σ_δ, the qubit linewidth [8,24,32]

$$\Gamma_2 = 2\pi\delta\nu_q = |\partial\nu_q/\partial\delta|\sigma_\delta/\sqrt{2}\hbar \qquad (1)$$

is indeed linear in $\partial\nu_q/\partial\delta$, with a minimum at $\delta = 0$ ("sweet spot").

The root-mean-square amplitude of the detuning noise, $\sigma_\delta \sim 0.19 \pm 0.02$ μeV, is found to be more than one order of magnitude lower than previously reported for semiconductor QDs [8,24].

To perform the time-resolved readout of the DQD qubit, we first determine the qubit state-dependent cavity frequency shift $\chi = g^2/\Delta_{r,q}$. For a coupling strength $g/2\pi \sim 55$ MHz and a frequency detuning $\Delta_{r,q}/2\pi \sim |5.680 - 5.075|$GHz, we expect $\chi/2\pi \sim 5$ MHz. We extract the resonator frequency from a measurement of the reflection coefficient with the qubit in the ground state $|g\rangle$ [blue trace in Figs. 4(a) and 4(b)]. Then, we apply a continuous coherent tone of duration $t_{\mathrm{dr}} \gg T_2$ at frequency $\nu_s = \nu_q(\delta = 0)$ saturating the qubit transition and creating a fully mixed qubit state ($P_g = P_e = 1/2$). Comparing the frequency of the resonator with the qubit in the fully mixed state [orange curve in Figs. 4(a) and 4(b)] to the one in the ground state $|g\rangle$, we extract the resonator frequency shift $\chi/2\pi \sim 5$ MHz [26], which matches the predicted value.

We coherently control the qubit quantum state by applying microwave pulses. We infer the qubit state by measuring the amplitude and phase response of the resonator [Fig. 4(c)], as in Refs. [33,34].

We record the time-dependent resonator response to the applied measurement microwave pulse with the qubit in the ground state $|g\rangle$ (blue trace) and when applying a microwave pulse to prepare its excited state $|e\rangle$ (red trace) [Fig. 4(c)]. We adjust the phase of the measurement pulse to maximize (minimize) the detected signal in the Q (I) quadrature. All measurements are performed at $\delta = 0$, where qubit coherence is best.

When applying the readout pulse with the qubit in $|g\rangle$, we observe an exponential rise of the resonator response reaching a steady state on a timescale of $\sim 1/\kappa$. In $|e\rangle$, the resonator frequency is shifted by 2χ resulting in a different Q quadrature response (red trace). The integrated area between the two curves in Fig. 4(c), averaged about 10^6 times, is proportional to the qubit excited state population P_e as discussed, e.g., in Refs. [33,34].

We apply microwave drive pulses to the DQD qubit at its transition frequency $\nu_{\mathrm{dr}} = \nu_q(\delta = 0) = 2t = 4.033$ GHz through the resonator. The qubit is detuned by $\Delta_{r,q} \sim 15g \gg \kappa_{\mathrm{tot}}$ from the resonator. We synthesize the Gaussian qubit control pulses directly (without up-conversion) by using an arbitrary waveform generator (AWG) with a 25 gigasamples/s sampling rate allowing for good pulse definition down to subnanosecond pulse length.

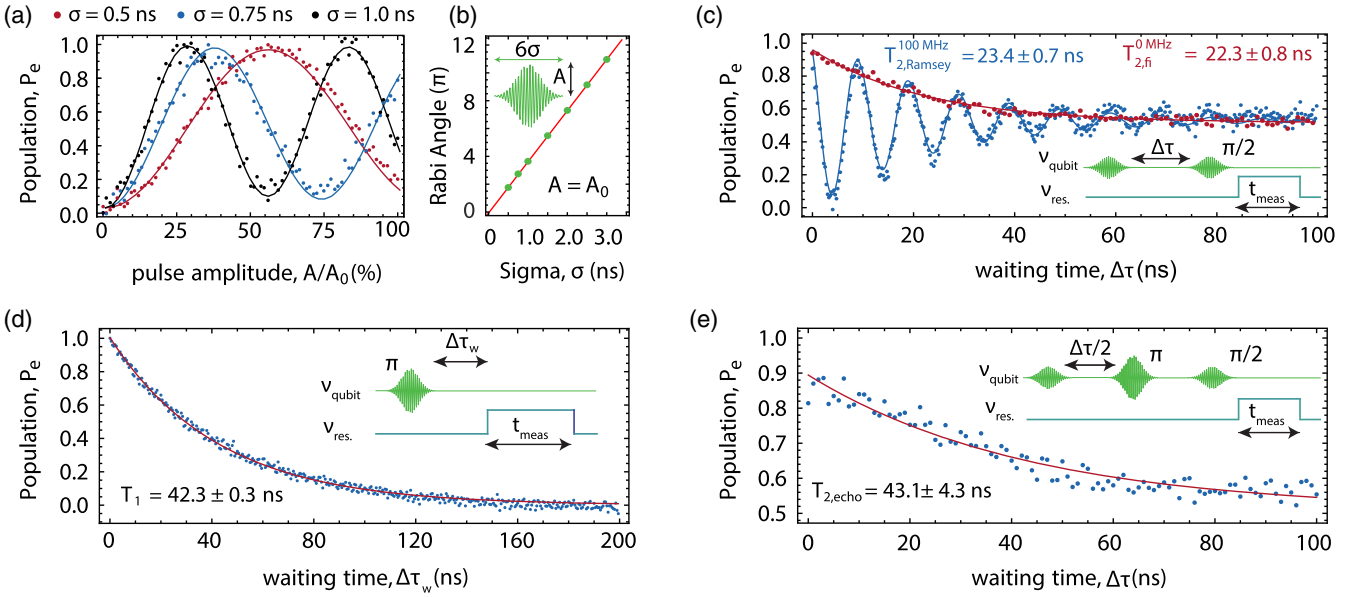

FIG. 5. Time-resolved measurements of the DQD qubit at $\nu_q(\delta = 0) = 2t = 4.033$ GHz. (a) Rabi oscillations for the indicated pulse widths versus pulse amplitude A ($A_0 \sim 150$ mV). A digitally synthesized example pulse as applied to the qubit is shown in the inset in (b). The solid line is the result of a master equation simulation accounting for qubit decoherence. (b) Measured Rabi angle (dots) for fixed pulse amplitude A_0 versus pulse length σ with a linear fit (red line). (c) Ramsey fringe measurement. The qubit excited state population P_e versus time difference $\Delta\tau$ separating the two $\pi/2$ pulses applied at the qubit frequency ν_q (red trace) and 100 MHz detuned (blue trace). The inset shows the pulse sequence. (d) Measurement of DQD qubit relaxation time T_1. A π pulse applied at the qubit frequency ν_q is followed by a readout pulse with delay $\Delta\tau_w$. (e) Spin-echo measurement. See the text for details. All data points are averaged 1.6 million times.

We observe Rabi oscillations in the DQD charge qubit excited state population P_e by applying pulses [see the inset in Fig. 5(b)] with standard deviation $\sigma \sim 0.5$, 0.75, and 1.0 ns versus normalized microwave pulse amplitudes A/A_0 followed by a pulsed dispersive readout as described above [Fig. 5(a)]. The fastest π-Rabi pulse, realized in our experiment by using the maximum available pulse amplitude $A_0 \sim 150$ mV at the AWG output, has a standard deviation of $\sigma \sim 0.25$ ns. This corresponds to a sizable Rabi frequency of up to ~800 MHz averaged over the pulse duration. We observe the expected linear dependence of the Rabi angle versus pulse length obtained for a fixed maximum pulse amplitude [Fig. 5(b)].

We determine the coherence time of the DQD charge qubit, configured as in Fig. 5(a), from a Ramsey fringe experiment using two $\pi/2$ pulses separated by a free evolution time $\Delta\tau$ followed by a readout pulse [inset, Fig. 5(c)]. Driving the qubit on resonance $\Delta_{q,\mathrm{dr}}/2\pi = \nu_q - \nu_{\mathrm{dr}} = 0$ (red curve) or $\Delta_{q,\mathrm{dr}}/2\pi = \nu_q - \nu_{\mathrm{dr}} = 100\,\mathrm{MHz}$ detuned (blue curve), we obtain a free induction decay time of $T_{2,\mathrm{fi}} \sim (22.3 \pm 0.8)$ ns or a Ramsey decay time of $T_{2,\mathrm{Ramsey}} \sim (23.4 \pm 0.7)$ ns when extracting the exponential decay coefficient from the data [Fig. 5(c)].

We determine the energy relaxation time $T_1 \sim (42.3 \pm 0.3)$ ns of the DQD charge qubit in the same configuration by initializing the qubit in $|e\rangle$ and varying the time $\Delta\tau_w$ before reading out the qubit state [Fig. 5(d)]. In this specific DQD configuration, $T_2 \ll 2T_1$, indicating that coherence is limited by pure dephasing. To investigate the origin of the low-frequency noise-limiting coherence, we also perform a Hahn-echo experiment by interleaving the Ramsey sequence with an extra π pulse in the middle [inset, Fig. 5(e)]. The echo decay time $T_{2,\mathrm{echo}} \sim (43.1 \pm 4.3)$ ns [Fig. 5(e)] is a factor of 2 longer than the $T_{2,\mathrm{Ramsey}}$ but still lower than $2T_1$, indicating that fluctuations faster than $\Delta\tau$ contribute to dephasing.

We reason that the unusually long charge coherence times extracted from both time-resolved and spectroscopic measurements of our device can be attributed to a combination of lower charge noise magnitude and reduced sensitivity to charge noise engineered by making use of QDs with a lower charging energy which are coupled more strongly by the interdot capacitance. The filters in the dc lines and the GaAs/AlGaAs heterostructure are the same as those used in Ref. [15]. The dephasing rate γ_ϕ of semiconductor quantum dot charge qubits is typically dominated by low-frequency fluctuations of the charge detuning parameter δ with $1/f$ spectral density [4,5,8,10]. For DQDs biased at the charge sweet spot $\delta = 0$, the dephasing is proportional to the square of the total charging energy E_c^2 [8,16,32], with $E_c = e^2/C_\Sigma$ and C_Σ the DQD total capacitance. Thus, devices with a larger interdot capacitance, i.e., smaller interdot charging energy, are affected less by charge noise, as argued in Ref. [35] for two coupled Cooper pair

boxes. In comparison to our previous work [15] $(E_{cL}, E_{cR}, E_m) \sim (202, 220, 99)$ GHz, the current device has charging energies for the left dot E_{cL} and the right dot E_{cR} which are a factor of 2 smaller and an interdot charging energy E_m on a similar scale (defined as in Refs. [3,35]), $(E_{\mathrm{cL}}, E_{\mathrm{cR}}, E_m) \sim (103, 100, 136)$ GHz. These two arguments support our observation of a tenfold reduction of effective detuning noise in this work in comparison to previous works [15].

Dispersive readout combined with all-microwave control of qubits is an essential feature of quantum information processing with superconducting circuits. We are convinced that the presented methods will contribute significantly to the continued improvement of tools and techniques for quantum information processing with charge and spin qubits in semiconductor nanostructures.

In particular, the methods presented here, together with the frequency tunability of the SQUID array resonator, do allow for a detailed study of coherence properties of charge qubits as a function of the interdot tunnel rate and detuning, in order to disentangle the effects of the qubit relaxation and dephasing. Furthermore, by introducing a parametric amplifier and a Purcell filter in the amplification chain (with optimized design) [36], we expect to achieve ultrafast high-fidelity single shot readout. Additionally, introducing an appropriately filtered DQD drive line will allow one to realize even larger drive rates, further reducing single qubit gate times and increasing gate fidelity.

We acknowledge useful discussions with Andreas Landig, Simon Stroz, Theodore Walter, Philipp Kurpiers, Anton Potočnik, Christian K. Andersen, and Johannes Heinsoo. We thank Alexandre Blais for valuable feedback on the manuscript. This work was supported by the Swiss National Science Foundation (SNF) through the National Center of Competence in Research (NCCR) Quantum Science and Technology (QSIT), the project Elements for Quantum Information Processing with Semiconductor/Superconductor Hybrids (EQUIPS), and by ETH Zurich.

P. S. and D. J. W. contributed equally to this work.

[1] D. Loss and D. P. DiVincenzo, Phys. Rev. A **57**, 120 (1998).
[2] L. P. Kouwenhoven, D. Austing, and S. Tarucha, Rep. Prog. Phys. **64**, 701 (2001).
[3] W. G. van der Wiel, S. De Franceschi, J. M. Elzerman, T. Fujisawa, S. Tarucha, and L. P. Kouwenhoven, Rev. Mod. Phys. **75**, 1 (2002).
[4] T. Hayashi, T. Fujisawa, H. D. Cheong, Y. H. Jeong, and Y. Hirayama, Phys. Rev. Lett. **91**, 226804 (2003).
[5] J. R. Petta, A. C. Johnson, C. M. Marcus, M. P. Hanson, and A. C. Gossard, Phys. Rev. Lett. **93**, 186802 (2004).
[6] J. R. Petta, A. C. Johnson, J. M. Taylor, E. A. Laird, A. Yacoby, M. D. Lukin, C. M. Marcus, M. P. Hanson, and A. C. Gossard, Science **309**, 2180 (2005).
[7] R. Hanson, L. P. Kouwenhoven, J. R. Petta, S. Tarucha, and L. M. K. Vandersypen, Rev. Mod. Phys. **79**, 1217 (2007).
[8] K. D. Petersson, J. R. Petta, H. Lu, and A. C. Gossard, Phys. Rev. Lett. **105**, 246804 (2010).
[9] O. E. Dial, M. D. Shulman, S. P. Harvey, H. Bluhm, V. Umansky, and A. Yacoby, Phys. Rev. Lett. **110**, 146804 (2013).
[10] E. Paladino, Y. M. Galperin, G. Falci, and B. L. Altshuler, Rev. Mod. Phys. **86**, 361 (2014).
[11] M. D. Reed, B. Maune, R. W. Andrews, M. G. Borselli, K. Eng, M. Jura, A. A. Kiselev, T. D. Ladd, S. T. Merkel, I. Milosavljevic *et al.*, Phys. Rev. Lett. **116**, 110402 (2016).
[12] F. Martins, F. K. Malinowski, P. D. Nissen, E. Barnes, S. Fallahi, G. C. Gardner, M. J. Manfra, C. M. Marcus, and F. Kuemmeth, Phys. Rev. Lett. **116**, 116801 (2016).
[13] A. Wallraff, D. I. Schuster, A. Blais, L. Frunzio, R.-S. Huang, J. Majer, S. Kumar, S. M. Girvin, and R. J. Schoelkopf, Nature (London) **431**, 162 (2004).
[14] X. Mi, J. V. Cady, D. M. Zajac, P. W. Deelman, and J. R. Petta, Science **355**, 156 (2017).
[15] A. Stockklauser, P. Scarlino, J. V. Koski, S. Gasparinetti, C. K. Andersen, C. Reichl, W. Wegscheider, T. Ihn, K. Ensslin, and A. Wallraff, Phys. Rev. X **7**, 011030 (2017).
[16] L. E. Bruhat, T. Cubaynes, J. J. Viennot, M. C. Dartiailh, M. M. Desjardins, A. Cottet, and T. Kontos, Phys. Rev. B **98**, 155313 (2018).
[17] X. Mi, M. Benito, S. Putz, D. M. Zajac, J. M. Taylor, G. Burkard, and J. R. Petta, Nature (London) **555**, 599 (2018).
[18] A. J. Landig, J. V. Koski, P. Scarlino, U. C. Mendes, A. Blais, C. Reichl, W. Wegscheider, A. Wallraff, K. Ensslin, and T. Ihn, Nature (London) **560**, 179 (2018).
[19] N. Samkharadze, G. Zheng, N. Kalhor, A. Brousse, D. Sammak, U. C. Mendes, A. Blais, G. Scappucci, and L. M. K. Vandersypen, Science **359**, 1123 (2018).
[20] Z. Shi, C. B. Simmons, D. R. Ward, J. R. Prance, R. T. Mohr, T. S. Koh, J. K. Gamble, X. Wu, D. E. Savage, M. G. Lagally *et al.*, Phys. Rev. B **88**, 075416 (2013).
[21] Y. Dovzhenko, J. Stehlik, K. D. Petersson, J. R. Petta, H. Lu, and A. C. Gossard, Phys. Rev. B **84**, 161302(R) (2011).
[22] B. Wang, B. Chen, G. Cao, H. Li, M. Xiao, and G. Guo, Europhys. Lett. **117**, 57006 (2017).
[23] D. Kim, D. R. Ward, C. B. Simmons, J. K. Gamble, R. Blume-Kohout, E. Nielsen, D. E. Savage, M. G. Lagally, M. Friesen, S. N. Coppersmith, and M. A. Eriksson, Nat. Nanotechnol. **10**, 243 (2015).
[24] B. Thorgrimsson, D. Kim, Y.-C. Yang, L. W. Smith, C. B. Simmons, D. R. Ward, R. H. Foote, J. Corrigan, D. E. Savage, M. G. Lagally, M. Friesen, S. N. Coppersmith, and M. A. Eriksson, npj Quantum Inf. **3**, 1 (2017).
[25] T. Frey, P. J. Leek, M. Beck, A. Blais, T. Ihn, K. Ensslin, and A. Wallraff, Phys. Rev. Lett. **108**, 046807 (2012).
[26] A. Blais, R.-S. Huang, A. Wallraff, S. M. Girvin, and R. J. Schoelkopf, Phys. Rev. A **69**, 062320 (2004).
[27] D. I. Schuster, A. Wallraff, A. Blais, L. Frunzio, R.-S. Huang, J. Majer, S. M. Girvin, and R. J. Schoelkopf, Phys. Rev. Lett. **94**, 123602 (2005).

[28] See Supplemental Material at http://link.aps.org/supplemental/10.1103/PhysRevLett.122.206802 for further details on the measurement setup and the device parameters, which includes Refs. [29–31].
[29] A. B. Zorin, Rev. Sci. Instrum. **66**, 4296 (1995).
[30] J. M. Chow, L. DiCarlo, J. M. Gambetta, F. Motzoi, L. Frunzio, S. M. Girvin, and R. J. Schoelkopf, Phys. Rev. A **82**, 040305(R) (2010).
[31] C. H. Wong and M. G. Vavilov, Phys. Rev. A **95**, 012325 (2017).
[32] G. Ithier, E. Collin, P. Joyez, P. J. Meeson, D. Vion, D. Esteve, F. Chiarello, A. Shnirman, Y. Makhlin, J. Schriefl, and G. Schön, Phys. Rev. B **72**, 134519 (2005).
[33] A. Wallraff, D. I. Schuster, A. Blais, L. Frunzio, J. Majer, M. H. Devoret, S. M. Girvin, and R. J. Schoelkopf, Phys. Rev. Lett. **95**, 060501 (2005).
[34] R. Bianchetti, S. Filipp, M. Baur, J. M. Fink, M. Göppl, P. J. Leek, L. Steffen, A. Blais, and A. Wallraff, Phys. Rev. A **80**, 043840 (2009).
[35] J. Q. You, X. Hu, and F. Nori, Phys. Rev. B **72**, 144529 (2005).
[36] T. Walter, P. Kurpiers, S. Gasparinetti, P. Magnard, A. Potočnik, Y. Salathé, M. Pechal, M. Mondal, M. Oppliger, C. Eichler, and A. Wallraff, Phys. Rev. Applied **7**, 054020 (2017).